Journal of Sound and Vibration (1997) **203**(2), 307–319

GROUND VIBRATION IN THE VICINITY OF A RECTANGULAR LOAD ACTING ON A VISCOELASTIC LAYER OVER A RIGID FOUNDATION

D. V. Jones

University of the West of England, Department of Mathematical Sciences, Coldharbour Lane, Frenchay, Bristol BS16 1QY, England

O. Laghrouche and D. Le Houedec

Ecole Centrale De Nantes, LMS, 1 Rue De La Noë, 44072 Nantes Cedex 03, France

AND

M. Petyt

ISVR, University of Southampton, Southampton SO17 1BJ, England

(*Received* 5 *July* 1996, *and in final form* 5 *December* 1996)

The transmission of vibrations in the vicinity of a rectangular harmonic vertical load, acting on a viscoelastic layer overlaying a rigid half-space, is investigated theoretically, using a semi-analytic approach. The solution involves a double Fourier transform with respect to two of the space variables of Navier's elastodynamic equations. The inverse double Fourier transform is achieved with the FFT algorithm. Results presented include transformed displacements in the wavenumber domain, actual displacements in the near-field of the load, and the direct receptance at the load.

1. INTRODUCTION

The original motivation for the work described in this paper was concern about vibrations caused by rail and road transport. Theoretical models which simulate the propagation of such vibration, will be of use in optimising the application of defensive measures such as trenches, or vibration absorbing material placed under either the source of vibration or a protected structure. The model of the load shape and ground structure used here is expected to more closely match experimental results for retangular loads, than a model which maintains cylindrical symmetry, or represents the ground as a half-space.

The ground is modelled as a viscoelastic layer overlying a rigid foundation, with an harmonic vertical load in the form of a rectangle. The load boundary condition is defined as a force rather than a displacement, to avoid mixed boundary conditions. A double Fourier transform is used to find the transformed displacements in the wavenumber domain; explicit expressions for the three components of transformed displacements are found as functions of the two transform variables, which are the wavenumbers in the two horizontal directions.

The work presented here is a natural extension of two previous papers by two of the present authors. In reference [1], the corresponding plane problem was studied, in which

0022–460X/97/220307 + 13 $25.00/0/sv960899

the load is modelled as an infinite strip acting on a layer over an inflexible foundation. The normal modes of free vibration, which are useful for interpreting the present results are also calculated. In reference [2], a three-dimensional problem of a rectangular load acting on a half-space was studied. Previous work relevant to these two problems was discussed in [1] and [2].

In most previous work involving three-dimensional modelling of the ground structure used here, the load has been modelled as either a point or a disc, to maintain cylindrical symmetry; see Girardi [3] for example. Recently Auersch [4] has considered a point load acting on an elastic layer overlying a flexible half-space. The finite element method is particularly well-suited to the ground model used in this paper, and has been used for example by Waas [5] and Jones *et al*. [6]. An application of the present work is in the verification of numerical methods such as finite elements and boundary elements, which can then be used to study more complex ground structures.

A review of work up to 1983 has been given by Gazetas [7].

2. FOURIER TRANSFORM OF THE DISPLACEMENTS

2.1. TRANSFORM OF NAVIER'S EQUATIONS

The model of the ground, co-ordinate system and load are shown in Figure 1. The rectangle has sides of length $2b$ and $2c$, and is aligned with respect to the co-ordinate axes as shown. It rests on an homogeneous, isotropic viscoelastic layer, with material properties E (Young's modulus), ρ (density) and v (Poisson ratio), which overlies a rigid foundation. The layer exhibits hysteric damping characterised by a loss factor η, and as a result the constants E, λ and μ (see equations (4) and (5) for the definitions of λ and μ) are each multiplied by a factor $(1 + i\eta)$; these constants are therefore complex. An harmonic vertical load acts uniformly over the rectangle, and no shear stresses exist at the surface. The behaviour of the layer is described by Navier's elastodynamic equations (see reference [8] Appendix A, for example). In the absence of a body force, and assuming the motion is harmonic, one obtains the following three equations for the components of displacement (u, v, w):

$$(\lambda + \mu)\frac{\partial \Delta}{\partial x} + \mu \nabla^2 u + \rho\omega^2 u = 0, \tag{1}$$

$$(\lambda + \mu)\frac{\partial \Delta}{\partial y} + \mu \nabla^2 v + \rho\omega^2 v = 0, \tag{2}$$

$$(\lambda + \mu)\frac{\partial \Delta}{\partial z} + \mu \nabla^2 w + \rho\omega^2 w = 0, \tag{3}$$

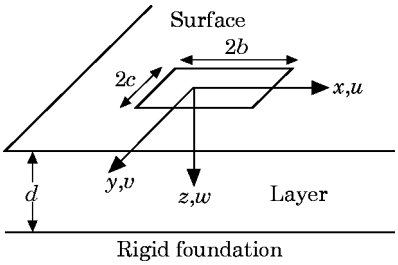

Figure 1. Diagram of the model.

in which λ and μ, the Lamé constants, are defined as

$$\lambda = vE(1 + i\eta)/(1 + v)(1 - 2v), \qquad \mu = E(1 + i\eta)/2(1 + v). \tag{4, 5}$$

In equations (1) to (3) ∇^2 is the Laplacian operator, and Δ is the dilatation, defined by

$$\Delta = \partial u/\partial x + \partial v/\partial y + \partial w/\partial z. \tag{6}$$

Differentiating equations (1) to (3) with respect to x, y and z respectively, dividing each equation by ρ and summing, gives

$$(\nabla^2 + k_1^2)\Delta = 0, \tag{7}$$

where $k_1 = \omega/c_1$ and $c_1^2 = (\lambda + 2\mu)/\rho$. To solve equation (7) the double Fourier transform is used and defined as

$$\bar{f}(\beta, \gamma, z) = \int_{-\infty}^{\infty} \int_{-\infty}^{\infty} f(x, y, z)\, e^{-i(\beta x + \gamma y)}\, dx\, dy. \tag{8}$$

With the above definition of the Fourier transform, the corresponding inverse transform will include a factor $1/(4\pi^2)$. Applying the Fourier transform to equation (7) yields a simple differential equation for the transform of the dilatation, the solution of which is

$$\bar{\Delta} = A\, e^{-\alpha_1 z} + B\, e^{\alpha_1 z}, \tag{9}$$

where

$$\alpha_1^2 = \beta^2 + \gamma^2 - k_1^2. \tag{10}$$

Substituting equation (9) into equations (1) to (3) and applying the Fourier transform, the resulting three equations can be expressed as

$$\left(\frac{d^2}{dz^2} - \alpha_2^2\right)\begin{pmatrix}\bar{u}\\ \bar{v}\\ \bar{w}\end{pmatrix} = \left(1 - \frac{k_2^2}{k_1^2}\right)\begin{pmatrix} i\beta(A\, e^{-\alpha_1 z} + B\, e^{\alpha_1 z})\\ i\gamma(A\, e^{-\alpha_1 z} + B\, e^{\alpha_1 z})\\ \alpha_1(-A\, e^{-\alpha_1 z} + B\, e^{\alpha_1 z})\end{pmatrix}, \tag{11}$$

where $k_2 = \omega/c_2$ and $c_2^2 = \mu/\rho$, and

$$\alpha_2^2 = \beta^2 + \gamma^2 - k_2^2. \tag{12}$$

Equation (11) was obtained using the result

$$(\lambda + \mu)/\mu = k_2^2/k_1^2 - 1. \tag{13}$$

The solution of equation (11) is

$$\begin{pmatrix}\bar{u}\\ \bar{v}\\ \bar{w}\end{pmatrix} = \begin{pmatrix}-i\beta\\ -i\gamma\\ \alpha_1\end{pmatrix}\frac{A}{k_1^2}\, e^{-\alpha_1 z} + \begin{pmatrix}-i\beta\\ -i\gamma\\ -\alpha_1\end{pmatrix}\frac{B}{k_1^2}\, e^{\alpha_1 z} + \begin{pmatrix}C\\ E\\ G\end{pmatrix} e^{\alpha_2 z} + \begin{pmatrix}D\\ F\\ H\end{pmatrix} e^{-\alpha_2 z}, \tag{14}$$

where $A, B, \ldots, H$ are functions of the wavenumbers β and γ. G and H are found in terms of the other unknowns by introducing the transform of the dilatation. Transforming equation (6) gives

$$\bar{\Delta} = \mathrm{i}\beta\bar{u} + \mathrm{i}\gamma\bar{v} + \mathrm{d}\bar{w}/\mathrm{d}z. \tag{15}$$

Substituting in equation (15) for the transformed displacements from equation (14), and equating to equation (9) leads to the following expressions for G and H:

$$G = (-\mathrm{i}/\alpha_2)(\beta C + \gamma E), \qquad H = (\mathrm{i}/\alpha_2)(\beta D + \gamma F). \tag{16, 17}$$

2.2. TRANSFORM OF STRESS-STRAIN RELATIONS

The stress-strain relations can be expressed in the form

$$\tau_{ij} = \lambda\delta_{ij}\Delta + \mu(\partial u_i/\partial x_j + \partial u_j/\partial x_i) \tag{18}$$

where τ_{ij} is the stress tensor, δ_{ij} is the Kronecker delta, and u_i and x_i are the ith components of the vectors (u, v, w) and (x, y, z) respectively. Transforming the three z components of the stress tensor, as defined by equation (18), gives

$$\bar{\tau}_{xz} = \mu(\mathrm{i}\beta\bar{w} + \mathrm{d}\bar{u}/\mathrm{d}z) \tag{19}$$

$$\bar{\tau}_{yz} = \mu(\mathrm{i}\gamma\bar{w} + \mathrm{d}\bar{v}/\mathrm{d}z) \tag{20}$$

$$\bar{\tau}_{zz} = (\lambda\bar{\Delta} + 2\mu\, d\bar{w}/\mathrm{d}z). \tag{21}$$

The stress components τ_{xz} and τ_{yz} are zero at the surface, while the component τ_{zz} at the surface can be written as

$$\tau_{zz}|_{z=0} = \begin{Bmatrix} -P/4bc & |x| < b, \quad |y| < c \\ 0 & \text{elsewhere} \end{Bmatrix} \tag{22}$$

P is the total force acting on the rectangle, and is equally distributed over it. Clearly the surface is modelled as being stress-free outside the rectangle. The Fourier transformation of equation (22) is

$$\bar{\tau}_{zz}|_{z=0} = -P \sin\beta b \sin\gamma c/bc\beta\gamma \tag{23}$$

Using equation (14) to replace $\bar{u}$, $\bar{v}$ and $\bar{w}$ in equations (19) to (21), evaluating the resulting expressions at $z = 0$, and using equation (23) for the component $\bar{\tau}_{zz}$, leads to the following three equations:

$$(2\mathrm{i}\alpha_1\beta/k_1^2)(A - B) + [(\beta^2 + \alpha_2^2)/\alpha_2](C - D) + (\beta\gamma/\alpha_2)(E - F) = 0 \tag{24}$$

$$(2\mathrm{i}\alpha_1\gamma/k_1^2)(A - B) + (\beta\gamma/\alpha_2)(C - D) + [(\gamma^2 + \alpha_2^2)/\alpha_2](E - F) = 0 \tag{25}$$

$$\left(\lambda - \frac{2\mu\alpha_1^2}{k_1^2}\right)(A + B) - 2\mu\mathrm{i}(\beta(C + D) + \gamma(E + F)) = -\frac{P \sin\beta b \sin\gamma c}{bc\beta\gamma} \tag{26}$$

In principle the zero displacement boundary condition at the bottom of the layer could be used with equation (14) to generate three further equations for the six unknowns $A, B, \ldots, F$, which could then be solved simultaneously with equations (24)–(26). However, this direct approach leads to formidable numerical problems. To avoid these difficulties, the layer is divided up into several sub-layers. A dynamic stiffness matrix is then deduced for each sub-layer and finally a global stiffness matrix for the entire physical layer constructed.

2.3. STIFFNESS MATRIX FOR A SUB-LAYER

Substituting (14) into equations (19) to (21), using equations (16), (17) to replace G and H and evaluating at $z = 0$ and $z = h$ gives

$$\bar{\boldsymbol{\tau}} = \mathbf{S}\mathbf{A}, \tag{27}$$

where

$$\bar{\boldsymbol{\tau}} = (-\bar{\tau}_{zx}(0),\ -\bar{\tau}_{zy}(0),\ -\mathrm{i}\bar{\tau}_{zz}(0),\ \bar{\tau}_{zx}(h),\ \bar{\tau}_{zy}(h),\ \mathrm{i}\bar{\tau}_{zz}(h))^{\mathrm{T}} \tag{28}$$

and

$$\mathbf{A} = (A \quad B \quad C \quad D \quad E \quad F)^{\mathrm{T}} \tag{29}$$

and $\mathbf{S}$ is the appropriate 6×6 matrix of coefficients. The vector $\bar{\boldsymbol{\tau}}$ is defined as in equation (28) to make the stiffness matrix symmetric.

Now evaluating equations (14) at $z = 0$ and $z = h$, and using equations (16) and (17) to replace G and H, gives

$$\bar{\mathbf{U}} = \mathbf{T}\mathbf{A}, \tag{30}$$

where

$$\bar{\mathbf{U}} = (\bar{u}(0), \bar{v}(0), \mathrm{i}\bar{w}(0), \bar{u}(h), \bar{v}(h), \mathrm{i}\bar{w}(h))^{\mathrm{T}} \tag{31}$$

and $\mathbf{T}$ is the appropriate matrix of coefficients. Combining equations (27) and (30), and introducing the stiffness matrix $\mathbf{C}$ such that

$$\mathbf{C} = \mathbf{S}\mathbf{T}^{-1} \tag{32}$$

gives

$$\bar{\boldsymbol{\tau}} = \mathbf{C}\bar{\mathbf{U}}. \tag{33}$$

The sub-layer stiffness matrix $\mathbf{C}$ was derived using the computer algebra package Maple [9]. Equation (33) is for a single sub-layer of depth h. A global equation for n layers, such that $d = nh$, can be assembled by the same process used in finite element analysis. Finally, the boundary conditions at $z = 0$ and $z = d$ are applied before solving.

3. SOLUTION FOR THE TRANSFORMED DISPLACEMENT

The global stiffness matrix is diagonally dominant and allows a straightforward solution for the vector $\bar{\mathbf{U}}$. Figures 2 to 5 show the functions $\bar{u}$, $\bar{v}$ and $\bar{w}$ plotted in the (β, γ)-plane, with the choices of parameters shown in Table 1. The material constants and layer depth have been chosen to agree with the free vibration work described in [1], which aids interpretation of the figures. A square load has been preferred for these transform domain plots to emphasize the symmetry of the transformed displacements. A relatively high frequency for ground vibration of 64 Hz has been used, because with the chosen ground parameters this allows the development of several propagating modes in the 7 m layer, which gives interesting behaviour in both domains.

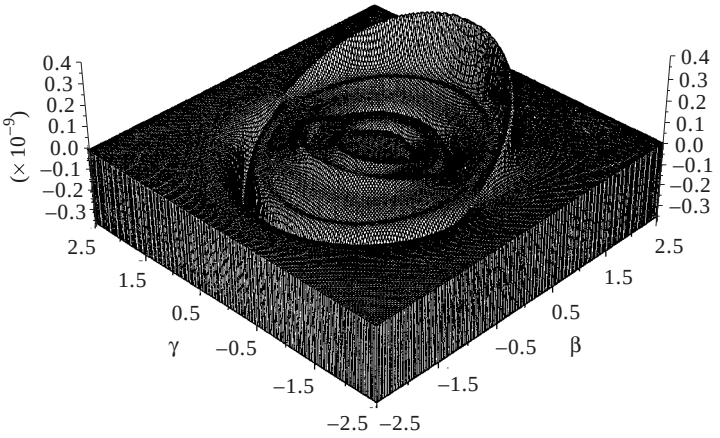

Figure 2. Real part of transformed horizontal displacements ($\bar{u}$).

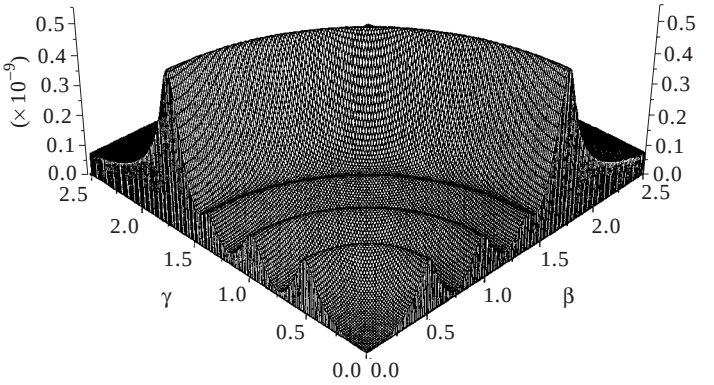

Figure 3. Amplitude of transformed vertical displacements ($\bar{w}$).

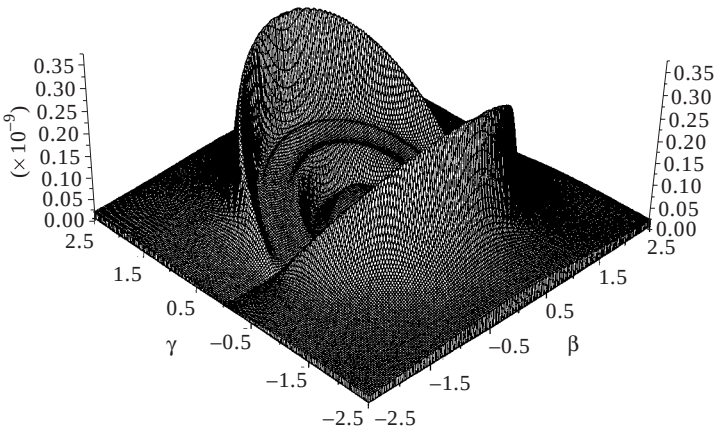

Figure 4. Amplitude of transformed transverse displacements ($\bar{v}$).

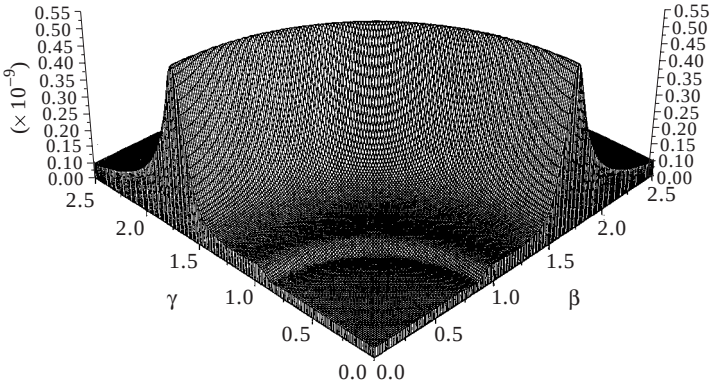

Figure 5. Amplitude of transformed vertical displacements ($\bar{w}$), $d = 70$ m..

Figure 2 shows the real part of the horizontal component of displacement, to illustrate the anti-symmetry of the function, whereas Figures 3–5 show the amplitude of the components, in order to incorporate real and imaginary parts in the same figures.

In Figure 2 one can see the real part of the component $\bar{u}$. This component is symmetric with respect to the plane $\gamma = 0$, and anti-symmetric with respect to $\beta = 0$. The peaks and troughs are located where the value of $(\beta^2 + \gamma^2)^{1/2}$ equals the wavenumber of one of the propagating modes in the layer, as calculated in reference [1]. In particular, one notes that the largest peak/trough is located close to the wavenumber k_R of the Rayleigh wave (for zero damping and with the parameters used here, $k_R = 1{\cdot}67\ \mathrm{m}^{-1}$). This is to be expected because for this combination of layer depth and frequency, the first mode is almost identical to the Rayleigh wave. One also notes that in the region $(\beta^2 + \gamma^2)^{1/2} > k_R$, $\bar{u}$ rapidly approaches zero, indicating that the inverse transform integrals may be truncated.

Figure 3 shows the component $\bar{w}$. Only the positive quarter-plane is shown because $\bar{w}$ is symmetric with respect to both the $\beta = 0$ and $\gamma = 0$ planes. Here one can see that the peaks are located at $(\beta^2 + \gamma^2)^{1/2} \simeq 0{\cdot}5$, $1{\cdot}0$, $1{\cdot}4$ and $1{\cdot}7$, as predicted by the free vibration analysis [1], and that the peak close to k_R is dominant.

Figure 4 shows the amplitude of the component $\bar{v}$. The component is zero along the γ-axis because of its antisymmetry (the surface appears symmetric because the amplitude is shown), and again one can see that outside the largest peak, $\bar{v}$ approaches zero rapidly.

TABLE 1

Parameters for Figures 2–5

Young's modulus	E (MN/m^2)	269
Density	ρ (kg/m^3)	1550
Poisson's ratio	ν	0·257
Damping coefficient	η	0·1
Total applied force	P (N)	1
Layer depth	d (m)	7†
Rectangle dimension	b (m)	0·3
Rectangle dimension	c (m)	0·3
Frequency of excitation	f (Hz)	64

† In Figure 5, $d = 70$ m.

Figure 5 should be compared with Figure 3. Both Figures show the component $\bar{w}$, but in the second one the depth of the layer is 70 m. It can be seen that for the shallower layer, the response is composed of the natural modes, whereas the deep layer behaves like a half-space: the large peak corresponds to the Rayleigh wave, and the peak near 1·0 on both axes is due to the compression wave. The influence of the shear wave is lost to the eye in the dominant Rayleigh peak.

These transform domain figures show that in layered ground with a frequency of excitation low enough for the layer interface to have an effect, which is usually the case in practice, it is a reasonable first approximation to only consider the Rayleigh wave, as if the ground were a half-space. However, the wavespeeds of the other components of the propagating disturbance would be poorly approximated by the shear and compression wavespeeds, as the *P* and *S* waves are "replaced" by natural modes which are the result of constructive interference of the body waves. In general these modes will not propagate at the shear or the compression wavespeeds.

4. NUMERICAL INVERSE TRANSFORMATION AND VERIFICATION OF RESULTS

To compute the inverse Fourier transform accurately using the Fast Fourier Transform (FFT) algorithm, the integrals must be truncated at sufficiently high values to avoid distortion of the results by aliasing, while the mesh of calculated function values must be fine enough to represent well the detail of the functions seen in Figures 2 to 5. It was found that an FFT over a grid of 2048 points by 2048 and a range of $-16 < \beta, \gamma < 16$ satisfied both these requirements. In the absence of comparable studies in the literature to verify the results, an alternative method of computing the inverse transform was used. Along the line $y = 0$ and for $z = 0$ it is convenient to use Filon's method of integrating oscillating integrals (see [10] for example). Figure 6 shows a comparison of results using the FFT and Filon's method with the parameters given in Table 2. These parameters were chosen for an eventual comparison with a finite element model, which has yet to be performed. To show the comparison in detail, the results have been "clipped" to a maximum value of $2{\cdot}0 \times 10^{-9}$ m; the maximum value at the centre of the load (not shown) was $23{\cdot}2 \times 10^{-9}$ m.

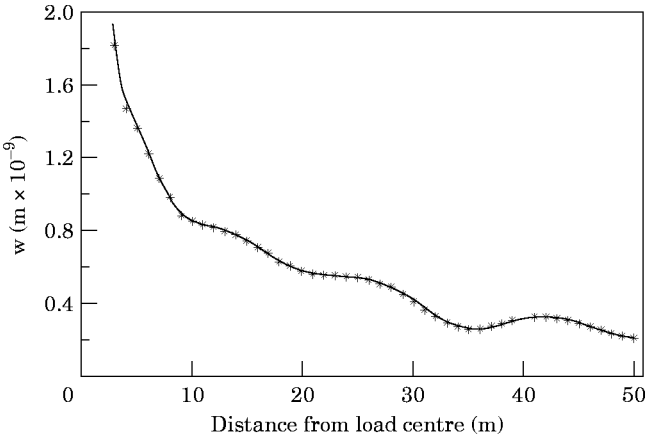

Figure 6. Comparison of two numerical methods using data in Table 2; ——, FFT; *, Filon method.

TABLE 2

Parameters for Figure 6

Young's modulus	E (MN/m^2)	46
Density	ρ (kg/m^3)	1700
Poisson's ratio	v	0·25
Damping coefficient	η	0·05
Total applied force	P (N)	1
Layer depth	d (m)	9.6
Rectangle dimension	b (m)	0.48
Rectangle dimension	c (m)	0.48
Frequency of excitation	f (Hz)	10

5. DISPLACEMENTS NEAR THE RECTANGULAR LOAD

The results presented in this section, which were all calculated using the FFT, are for the ground parameters shown in Table 1, but with a rectangular load of dimensions $b = 0{\cdot}75$, $c = 0{\cdot}125$. They can be divided into three groups: (1) the amplitudes of vertical and horizontal components of displacements along the surface for $y = 0$, and for the frequencies 16 Hz and 64 Hz (Figures 7 to 10); (2) the direct receptance at the centre of the rectangle (Figure 11); and (3) the amplitudes of horizontal and vertical components of displacements over the (x, y)-plane, plotted as surfaces, for 16 and 64 Hz and up to 25 m from the load (Figures 12 to 15). The two frequencies were specifically chosen because of the ground parameters used here: 16 Hz is close to the first resonant frequency of the layer, as predicted by the free vibration analysis [1], and as can be seen from the receptance graph in Figure 11, and 64 Hz is high enough to allow the development of several propagating modes in the layer, leading to constructive and destructive interference. Figure 7 shows the amplitude of the horizontal component up to 10 m from the load. This component is zero at the centre of the load, and reaches a maximum at the load edge, 0·75 m from the centre. The resonant frequency 16 Hz produces greater displacements in the near-field than 64 Hz, while the higher frequency produces a wavy profile because of interference of the propagating modes; this interference is more easily seen in Figure 8, which is the same as Figure 7 but over 50 m. Here one can see that destructive interference results in a near-zero response for 16 Hz about 21 m from the load.

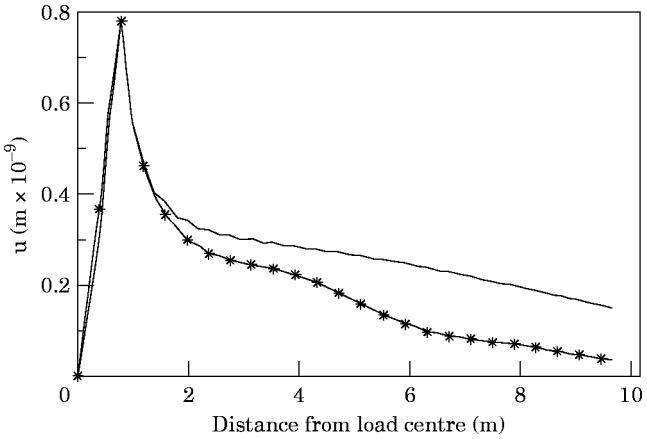

Figure 7. Horizontal displacements along $y = 0$ for 16 and 64 Hz over 10 m; ——, 16 Hz; ∗——∗, 64 Hz.

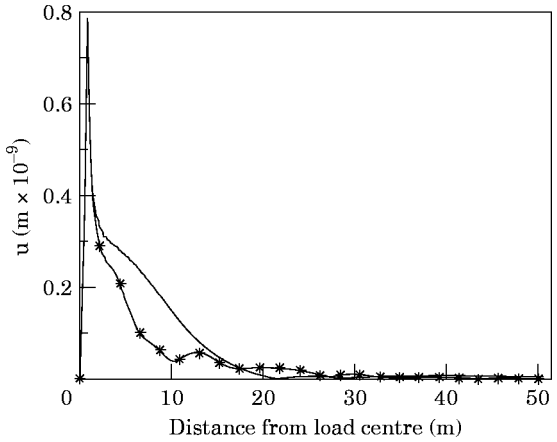

Figure 8. Extension of Figure 7 to 50 m. Key as Figure 7.

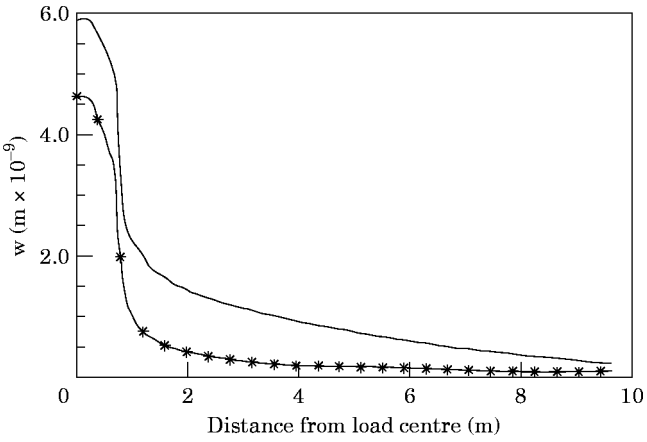

Figure 9. Vertical displacements along $y = 0$ for 16 (——) and 64 (∗——∗) Hz over 10 m.

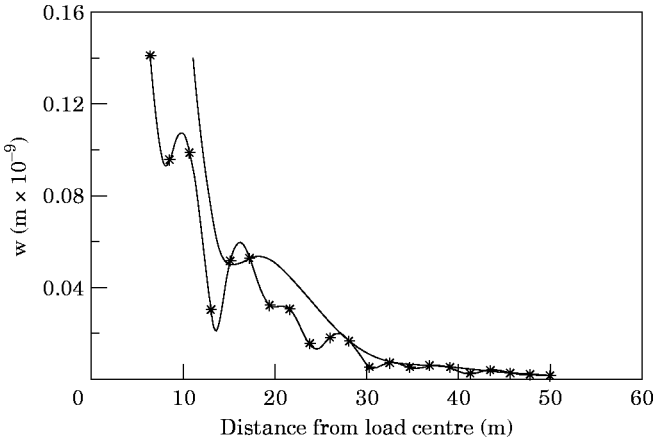

Figure 10. Extension of Figure 9 to 50 m. Key as Figure 9.

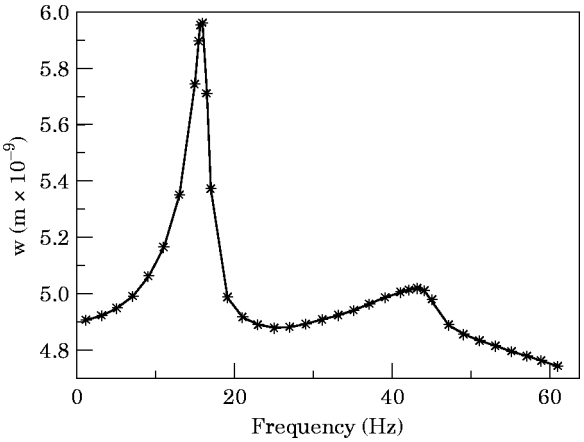

Figure 11. Direct vertical receptance for the rectangular load; the points marked with an asterix show the data, joined by straight line segments.

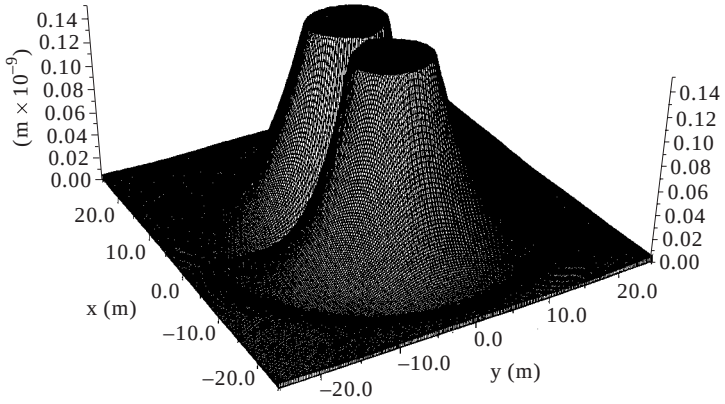

Figure 12. Amplitude of horizontal displacements (component u) for 16 Hz, "clipped" to show detail.

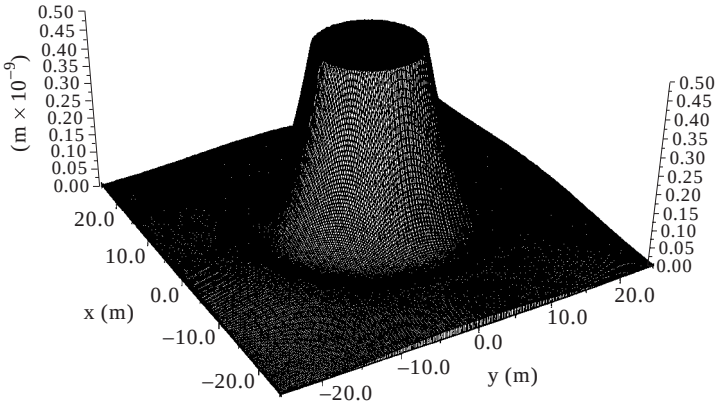

Figure 13. Amplitude of vertical displacements (component w) for 16 Hz, "clipped" to show detail.

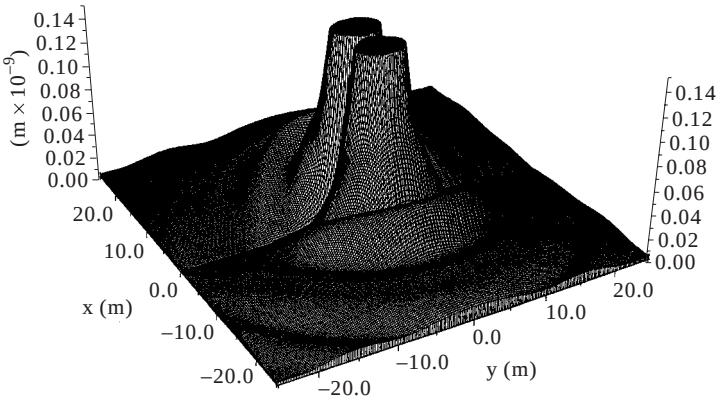

Figure 14. Amplitude of horizontal displacements (component u) for 64 Hz, "clipped" to show detail.

Figures 9 and 10 are equivalent to the two preceding figures, but show the amplitude of the vertical component. As might be expected for a vertically acting load, the vertical response is the largest component. The maximum response is near the centre of the load, and the load edge corresponds to a sharp decrease in amplitude. The response for 16 Hz dominates that for 64 Hz in the near-field, but Figure 10 shows that the interference of the propagating modes results in a region about 17 m from the load where the response to 64 Hz is the greater of the two. At 64 Hz five propagating modes exist, compared with only two at 16 Hz, which explains the greater waviness of the higher frequency response.

Figure 11 shows the direct receptance at the centre of the load, i.e. the amplitude of the vertical component at the origin. Two resonance peaks are evident. It was shown in reference [1] that the larger one corresponds to the phenomenon of two modes sharing the same wavenumber at that frequency, whilst the second peak near 44 Hz is caused by the fourth mode propagating with two distinct wavenumbers for a small frequency range near 44·8 Hz. It should be noted that both features are a result of the boundary condition of zero displacement at the bottom of the layer. Such behaviour could only be expected in practice in the case of a layer overlying a very much stiffer foundation.

Figures 12 to 15 show the vertical and horizontal components of displacement as surfaces. These figures have been "clipped" to show more detail. The actual maxima are, in the order they appear, 0·79, 5·90, 0·78 and 4·62, all $\times 10^{-9}$ m. Comparing these last four

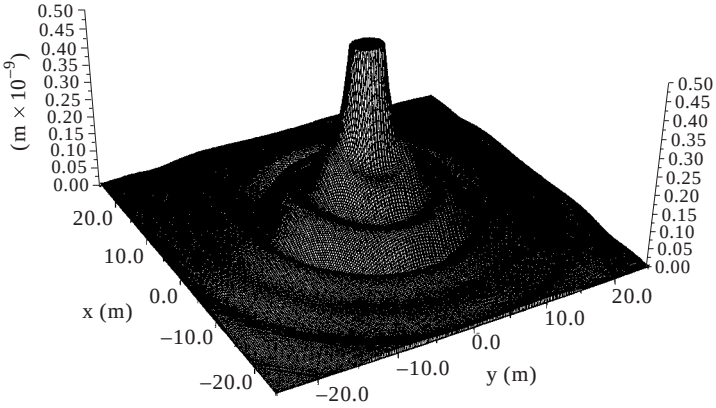

Figure 15. Amplitude of vertical displacements (component w) for 64 Hz, "clipped" to show detail.

figures, it is clear that the near-resonant frequency 16 Hz produces a much larger response near to the load than 64 Hz. The two figures for 64 Hz show the pattern of peaks and troughs produced by interference of the propagating modes. In Figures 12 and 14, which show the horizontal component at the two frequencies, the response is zero along the line $x = 0$, as required physically.

6. CONCLUSIONS

A theoretical model of ground vibrations caused by an harmonic, vertical and rectangular load acting on a viscoelastic layer over a rigid foundation has been developed. Results produced with the model have been verified by computing the inverse Fourier transforms of the exact expressions for the transformed displacements using two distinct methods, the Fast Fourier Transform and Filon's method. The results presented show the form of the transformed displacements, the amplitudes of the components of actual surface displacements along the line $x = 0$, and also plotted as surfaces over the (x, y) plane, and the direct receptance of the rectangular load. Resonance and interference features have been explained with reference to an earlier free vibration analysis of the propagating modes in the layer.

ACKNOWLEDGMENT

David Jones acknowledges the support of the Region des Pays de la Loire which provided him with a post-doctoral research grant to work with his co-authors in Nantes.

REFERENCES

1. D. V. Jones and M. Petyt 1992 *Journal of Sound and Vibration* **152**, 501–515. Ground vibration in the vicinity of a strip load: an elastic layer on a rigid foundation.
2. D. V. Jones and M. Petyt 1993 *Journal of Sound and Vibation* **166**, 141–159. Ground vibration in the vicinity of a rectangular load on a half-space.
3. L. Girardi 1981 *Annales de l'ITBTP*, *Sols et Fondations* **397**, 31–66. Propagation des vibrations dans les sols homogènes ou stratifiés.
4. L. Auersch 1994 *Journal of Sound and Vibration* **173**, 233–264. Wave propagation in layered soils: theoretical solution in wavenumber domain and experimental results of hammer and railway traffic excitation.
5. G. Waas 1972 *Ph.D. Thesis*, *University of California*, *Berkeley*. Linear two dimensional analysis of soil dynamics problems in semi-infinite layered media.
6. D. V. Jones, O. Laghrouche, D. Le Houedec 1996 *Proceedings of The Third International Conference on Computational Structures Technology*, *August*, *Budapest*, Pergamon Press–Elsevier Science. Three dimensional finite and infinite elements coupled model for traffic active isolation study.
7. G. Gazetas 1983 *International Journal of Soil Dynamics and Earthquake Engineering* **2**, 2–42. Analysis of machine foundations vibrations: state of the art.
8. K. F. Graff 1975 *Wave Motion in Elastic Solids*. Oxford: Clarendon Press.
9. D. Redfern 1994 *The Maple Handbook*. New York: Springer-Verlag.
10. J. E. Luco 1976 *Nuclear Engineering and Design* **36**, 325–340. Vibrations of a rigid disc on a layered viscoelastic medium.